The Astrophysical Journal Supplement Series, 241:34 (16pp), 2019 April https://doi.org/10.3847/1538-4365/ab074f

The Sloan Digital Sky Survey Reverberation Mapping Project: Sample Characterization

Yue Shen[1,2,19], Patrick B. Hall[3], Keith Horne[4], Guangtun Zhu[5], Ian McGreer[6], Torben Simm[7], Jonathan R. Trump[8], Karen Kinemuchi[9], W. N. Brandt[10,11,12], Paul J. Green[13], C. J. Grier[6,10], Hengxiao Guo[2], Luis C. Ho[14,15], Yasaman Homayouni[8], Linhua Jiang[14,15], Jennifer I-Hsiu Li[1], Eric Morganson[2], Patrick Petitjean[16], Gordon T. Richards[17], Donald P. Schneider[10,11], D. A. Starkey[1,4], Shu Wang[1,14], Ken Chambers[18], Nick Kaiser[18], Rolf-Peter Kudritzki[18], Eugene Magnier[18], and Christopher Waters[18]

[1] Department of Astronomy, University of Illinois at Urbana-Champaign, Urbana, IL 61801, USA; shenyue@illinois.edu
[2] National Center for Supercomputing Applications, University of Illinois at Urbana-Champaign, Urbana, IL 61801, USA
[3] Department of Physics and Astronomy, York University, Toronto, ON M3J 1P3, Canada
[4] SUPA Physics and Astronomy, University of St Andrews, Fife, KY16 9SS, UK
[5] Department of Physics and Astronomy, Johns Hopkins University, 3400 North Charles Street, Baltimore, MD 21218, USA
[6] Steward Observatory, University of Arizona, 933 North Cherry Avenue, Tucson, AZ 85721-0065, USA
[7] Max-Planck Institute for Extraterrestrial Physics, Giessenbachstrasse, Postfach 1312, D-85741, Garching, Germany
[8] University of Connecticut, Department of Physics, 2152 Hillside Road, Unit 3046, Storrs, CT 06269-3046, USA
[9] Apache Point Observatory and New Mexico State University, P.O. Box 59, Sunspot, NM 88349-0059, USA
[10] Department of Astronomy & Astrophysics, The Pennsylvania State University, University Park, PA 16802, USA
[11] Institute for Gravitation and the Cosmos, The Pennsylvania State University, University Park, PA 16802, USA
[12] Department of Physics, 104 Davey Lab, The Pennsylvania State University, University Park, PA 16802, USA
[13] Harvard-Smithsonian Center for Astrophysics, 60 Garden Street, Cambridge, MA 02138, USA
[14] Department of Astronomy, School of Physics, Peking University, Beijing 100871, People's Republic of China
[15] Kavli Institute for Astronomy and Astrophysics, Peking University, Beijing 100871, People's Republic of China
[16] Institut d'Astrophysique de Paris, Sorbonnes Universités, CNRS, 98bis, Boulevard Arago, F-75014 Paris, France
[17] Department of Physics, Drexel University, 3141 Chestnut Street, Philadelphia, PA 19104, USA
[18] Institute for Astronomy, University of Hawaii at Manoa, Honolulu, HI 96822, USA
Received 2018 October 25; revised 2019 January 23; accepted 2019 January 28; published 2019 April 15

Abstract

We present a detailed characterization of the 849 broad-line quasars from the Sloan Digital Sky Survey Reverberation Mapping (SDSS-RM) project. Our quasar sample covers a redshift range of $0.1 < z < 4.5$ and is flux-limited to $i_{\rm PSF} < 21.7$ without any other cuts on quasar properties. The main sample characterization includes: (1) spectral measurements of the continuum and broad emission lines for individual objects from the coadded first-season spectroscopy in 2014, (2) identification of broad and narrow absorption lines in the spectra, and (3) optical variability properties for continuum and broad lines from multi-epoch spectroscopy. We provide improved systemic redshift estimates for all quasars and demonstrate the effects of the signal-to-noise ratio on the spectral measurements. We compile measured properties for all 849 quasars along with supplemental multi-wavelength data for subsets of our sample from other surveys. The SDSS-RM sample probes a diverse range in quasar properties and shows well-detected continuum and broad-line variability for many objects from first-season monitoring data. The compiled properties serve as the benchmark for follow-up work based on SDSS-RM data. The spectral fitting tools are made public along with this work.

Key words: black hole physics – galaxies: active – line: profiles – quasars: general – surveys

Supporting material: FITS file

1. Introduction

The Sloan Digital Sky Survey Reverberation Mapping (SDSS-RM) project is a dedicated multi-object RM campaign that simultaneously monitors 849 quasars that cover a wide redshift and luminosity range with moderate-cadence imaging and spectroscopy (for a technical overview of the SDSS-RM project, see Shen et al. 2015a). Starting in 2014, SDSS-RM will continue through 2020 to build a spectroscopic time baseline of seven years, and a photometric time baseline of a decade when combining dedicated SDSS-RM imaging (2014–2020) with earlier (2010–2013) imaging from the Panoramic Survey Telescope and Rapid Response System (Pan-STARRS) 1 (PS1; Kaiser et al. 2010) survey.

The primary science goal of SDSS-RM is to measure RM lags between continuum flux and broad emission-line flux (e.g., Blandford & McKee 1982; Peterson 1993), which provide an estimate of the typical size of the broad-line region (BLR). Combining the measured RM lag and the width of the broad emission lines, one can estimate a "virial" mass of the central black hole (BH) assuming the BLR is virialized. RM is the primary technique to measure BH masses in active galaxies, and it anchors the so-called "single-epoch" BH mass estimators (for a review, see, e.g., Shen 2013), where the latter have been extensively used in the field to estimate quasar BH masses at all redshifts with single-epoch spectroscopy. SDSS-RM aims to extend previous RM studies that were limited to low-z and mostly low-luminosity active galactic nuclei (AGN) to both higher redshifts and a more representative sample by targeting a flux-limited ($i < 21.7$) quasar sample at $0.1 < z < 4.5$ without any cuts on quasar properties. The multiplex capability of SDSS-RM greatly improves the efficiency of RM, and our 2014 data set already led to lag detections that expand the redshift–luminosity range of RM measurements (e.g., Shen et al. 2016b; Grier et al. 2017; Li et al. 2017).

[19] Alfred P. Sloan Research Fellow.

In addition to lag measurements, the multi-epoch images and spectroscopy from SDSS-RM enable a diverse range of applications from host galaxy properties to accretion disk properties (e.g., Grier et al. 2015; Matsuoka et al. 2015; Shen et al. 2015b, 2016a; Sun et al. 2015, 2018; Denney et al. 2016a, 2016b; Li et al. 2017; Homayouni et al. 2018; Yue et al. 2018). The SDSS-RM field also has extensive multi-wavelength coverage from previous surveys and our dedicated follow-up programs. The SDSS-RM sample is a representative sample of quasars over a broad range of redshifts and physical parameters. As such, it is a highly valuable data set for quasar science, and a detailed characterization of the sample properties will be beneficial to many follow-up studies of the SDSS-RM sample.

In this work, we present a detailed characterization and compilation of quasar properties for the SDSS-RM sample. In Section 2, we describe the sample and the data. In Section 3, we detail our spectral characterization of the sample. In Section 4, we describe our optical variability characterization. We describe our compiled catalogs in Section 5 and summarize in Section 6. Additional information regarding our spectral fitting code is provided in the Appendix. Throughout this paper, we adopt a flat ΛCDM cosmology with $\Omega_\Lambda = 0.7$ and $h = 0.7$.

2. Data

2.1. Sample Overview

The SDSS-RM field is a single 7 deg^2 field that coincides with the PS1 Medium Deep Field (MDF. Tonry et al. 2012a) MD07 (R.A. J2000 = 213.704, decl. J2000 = +53.083), which lies within the CFHT-LS W3 field.[20]

The SDSS-RM sample contains 849 broad-line quasars over a redshift range of $0.1 < z < 4.5$. Most of the SDSS-RM quasars were previously spectroscopically confirmed quasars in SDSS-I–III. In particular, the SDSS-III Baryon Oscillation Spectroscopic Survey (BOSS; Dawson et al. 2013) targeted and spectroscopically confirmed most of these quasars. As detailed in Ross et al. (2012), the BOSS quasar survey combines optical color selection with a variety of ancillary target selection criteria to increase the total number of quasars. All objects classified as point-like and have magnitudes of $g < 22$ or $r < 21.85$ are passed to the quasar target selection code. A small number of quasars were added to the sample that were missed from SDSS; these objects were targeted with optical variability (55 quasars) and multi-wavelength selection (seven quasars) with follow-up spectroscopic confirmation (see details in Section 3.1 of Shen et al. 2015a). Table 2 provides the original target flags used in SDSS to select these quasars, which follow the same definitions as in the SDSS-I–III surveys, and a flag "OTHER_TARGET" to indicate additional target selection. The SDSS-RM quasar sample is intended to be a nearly complete, flux-limited sample of unobscured broad-line quasars, without any other cuts on multi-wavelength properties, emission-line properties, or variability properties. With additional target selection using optical variability or mid-infrared photometry from the *Wide-field Infrared Survey Explorer* (*WISE*) survey (Wright et al. 2010), the SDSS-RM sample is more complete in optical color space contaminated by stars (e.g., Schmidt et al. 2010; Morganson et al. 2015) and is less biased against dust-reddened type 1 quasars (e.g., Assef et al. 2013) than optical-only color selection. Nevertheless, obscured type 2 quasars without broad emission lines are apparently excluded from our sample, and some heavily dust-reddened quasars with peculiar colors may still be missing from our sample.

[20] http://www.cfht.hawaii.edu/Science/CFHTLS/

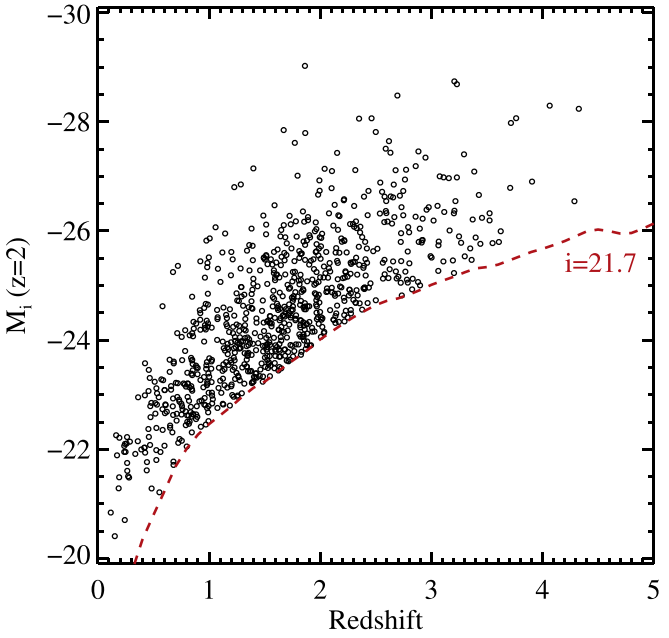

Figure 1. Distribution of the SDSS-RM quasar sample in the redshift–luminosity space. We use the emission-line flux corrected, absolute *i*-band magnitude normalized at $z = 2$ (equivalent to the rest-frame 2500 Å luminosity) as the luminosity indicator, following Richards et al. (2006b). The formal flux limit of the SDSS-RM sample is $i = 21.7$ (PSF magnitude, uncorrected for Galactic extinction).

Figure 1 displays the redshift–luminosity distribution of the SDSS-RM sample. Following Richards et al. (2006b), we use the emission-line corrected, absolute *i*-band magnitude normalized at $z = 2$ (equivalent to the rest-frame 2500 Å luminosity), $M_i(z = 2)$, as the continuum luminosity indicator. The conversion between $M_i(z = 2)$ and the conventional magnitude $M_i(z = 0)$ is (Richards et al. 2006b, their Equation (1)) $M_i(z = 0) = M_i(z = 2) + 0.596$. The formal flux limit of the sample is $i < 21.7$ (point-spread function (PSF) magnitude, uncorrected for Galactic extinction). There is a deficit of targets near the flux limit at low redshifts, due to the incomplete target selection in this regime as the main quasar target selection in BOSS was biased against extended sources (Ross et al. 2012). Compared to earlier RM samples that predominately focus on low-redshift and low-luminosity AGN, the SDSS-RM sample covers a much broader and contiguous range in the redshift and luminosity space, spanning almost all of the cosmic time and range from Seyferts ($M_i(z = 2) \gtrsim -22.5$ or $L_{\rm bol} \lesssim 10^{45}$ erg s^{-1}) to luminous quasars.

2.2. SDSS-RM Optical Imaging and Spectroscopy

The primary spectroscopy has been obtained with the SDSS telescope (Gunn et al. 2006) and the BOSS spectrographs (Smee et al. 2013). The first-season SDSS-RM spectroscopic data were taken from 2014 January to July in SDSS-III (Eisenstein et al. 2011) and consist of a total of 32 epochs with an average cadence of ∼4 days; each epoch had a typical exposure time of 2 hr. The SDSS-RM program has continued in

SDSS-IV (Blanton et al. 2017), with ∼12 epochs per year (2 per month) with a nominal exposure time of 1 hr each during 2015–2017 and ∼6 epochs per year (monthly cadence) during 2018–2020. As of 2018 July, we have obtained a total of 78 spectroscopic epochs and a spectroscopic baseline of 5 yr (2014–2018). The wavelength coverage of BOSS spectroscopy is ∼3650–10400 Å, with a spectral resolution of $R \sim 2000$. The typical signal-to-noise ratio (S/N) per 69 km s^{-1} pixel averaged over the g band in a 2 hr exposure is ∼4.5 at $g_{\rm psf} = 21.2$, but could be lower for epochs observed with poor observing conditions.

We obtained additional spectroscopic data with the Multiple Mirror Telescope (MMT)/Hectospec in 2017 in order to test the feasibility of continuing the spectroscopic monitoring with other facilities, which covers most of the RM targets in our sample as well as ancillary science targets, such as high-z quasar candidates and variable stars. These data will be presented elsewhere.

Supporting photometric observations in both the g and i bands have been obtained primarily with the Steward Observatory Bok 2.3 m telescope on Kitt Peak and the 3.6 m Canada–France–Hawaii Telescope (CFHT) on Maunakea, which roughly cover the same monitoring period as SDSS-RM spectroscopy with a cadence of ∼2 days in 2014 and reduced cadences in successive years. Details of the photometric observations and the subsequent data processing will be presented by K. Kinemuchi et al. (2019, in preparation). In addition, we also have early multi-band photometric light curves from PS1 during 2010–2013 with a typical cadence of several days. These early PS1 light curves substantially extend the photometric baseline of SDSS-RM and are critical to measuring long lags (e.g., on multi-year timescales) when combined with the later SDSS-RM spectroscopy. The SDSS-RM field continues to be monitored with the PS1 system in five bands since 2016, albeit with reduced cadence (about weekly to monthly per band).

By the end of the program in 2020, SDSS-RM will have a time baseline of a decade for imaging and seven years for spectroscopy.

2.3. Other Multi-wavelength Data

The SDSS-RM field is covered by several wide-area sky surveys, such as the *WISE* survey (Wright et al. 2010) and the Faint Images of the Radio Sky at Twenty cm (FIRST) radio survey (White et al. 1997). We compile the *WISE* photometry from the AllWISE release, as well as forced *WISE* photometry at the positions of SDSS sources (unWISE; Lang et al. 2016).

For the FIRST radio matches, we follow the procedures in Jiang et al. (2007) and Shen et al. (2011): we match the SDSS-RM quasars with the FIRST source catalog (2017 December 14 version) with a matching radius of 30″ and estimate the radio loudness as $R = f_{6\,\rm cm}/f_{2500}$, where $f_{6\,\rm cm}$ and f_{2500} are the flux density (f_ν) at rest-frame 6 cm and 2500 Å, respectively. For quasars with only one FIRST source within 30″, we match them again to the FIRST catalog with a matching radius of 5″ and classify the matched ones as core-dominant radio quasars. Quasars with multiple FIRST source matches within 30″ are classified as lobe-dominated. The rest-frame 6 cm flux density is determined from the FIRST integrated flux density at 20 cm assuming a power-law slope of $\alpha_\nu = -0.5$; the rest-frame 2500 Å flux density is determined from our spectral fits. For lobe-dominated radio quasars, we use all of the matched FIRST sources to compute the radio flux density.

The SDSS-RM field also overlaps with several extragalactic multi-wavelength fields, notably the All-wavelength Extended Growth strip International Survey (AEGIS) field (Davis et al. 2007). We have collected public multi-wavelength data for a subset of SDSS-RM quasars. These data include the multi-wavelength data from Nandra et al. (2015) for 32 SDSS-RM quasars, and *Spitzer* Infrared Array Camera (IRAC) and Multi-band Imaging Photometer (MIPS) data from the *Spitzer* Enhanced Imaging Products (SEIP) source list for 176 SDSS-RM quasars. Since these data apply only to a small subset of the SDSS-RM sample, we provided these compiled data in separate ancillary table files and archived them on the SDSS-RM data server.[21]

Finally, there are Galaxy Evolution Explorer (GALEX) near-ultraviolet (NUV) light curves and coadded imaging data for about half of the SDSS-RM sample from the GALEX Time Domain Survey (Gezari et al. 2013), United Kingdom Infrared Telescope (UKIRT) near-infrared imaging for the RM field, and X-ray data from various *XMM-Newton* and *Chandra* programs. In particular, we have obtained *XMM-Newton* imaging for the entire SDSS-RM field and are compiling X-ray properties for the sample. We will compile these future data sets when they become available and will distribute through the SDSS-RM data server.

3. Spectral Characterization

To measure the continuum and line fluxes from the spectra, we use a spectral fitting approach similar to our earlier work (e.g., Shen et al. 2008b, 2011; Shen & Liu 2012) but with a number of modifications, which we describe in detail below.

In this work, we use the coadded 2014 spectra (32 epochs in total). The 32 epochs were coadded using the SDSS-III spectroscopic pipeline `idlspec2d`, to produce high S/N individual spectra for all 849 quasars in the SDSS-RM sample. The coadded spectra have identical format as other SDSS-III spectra, with a logarithmic wavelength binning of 10^{-4} in $\log_{10}\lambda$ and are stored in vacuum wavelengths.

3.1. Spectral Fitting

We fit the coadded spectra[22] from the first-season (2014) observations with a continuum+emission-line model. The high signal-to-noise ratio (S/N) of the coadded spectra for individual objects allows measurements of weak emission lines, and these measurements represent the average properties of the quasar during this monitoring period. The fitting was performed in the rest frame of the quasar using the pipeline redshift, after correcting for Galactic reddening using the dust map in Schlegel et al. (1998) and the extinction curve from Cardelli et al. (1989).

The continuum fit was performed for all pixels in a set of relatively line-free (except for broad-band Fe II emission) windows over the entire spectrum of the quasar. The continuum model is described by a power law plus a third-order polynomial, where the additive (positive-definite) polynomial component is introduced to fit objects with peculiar (e.g., bending) continuum shapes that are likely caused by peculiar intrinsic dust reddening (see an example in Figure 5, top left

[21] ftp://quasar.astro.illinois.edu/public/sdssrm/paper_data/Sample_char/

[22] The coadded spectra are distributed on the SDSS-RM data server and are compiled in a single file (spPlate-0000-56837.fits) with the same format as other SDSS plates, where the fiber number corresponds to RMID+1 of the sample (Shen et al. 2015a).

panel). In addition to the continuum, we fit the optical and UV Fe II emission using empirical templates from the literature (e.g., Boroson & Green 1992; Vestergaard & Wilkes 2001; Tsuzuki et al. 2006; Salviander et al. 2007). The continuum and the Fe II emission form a pseudo-continuum, which is subtracted from the spectrum to form a line-only spectrum for which we measure emission-line properties. We do not include a Balmer continuum component in the fit because fitting such a feature requires sufficient wavelength coverage that is not available for most of our quasars; but our fitting code implements such a feature, which can be switched on and off. We also do not include a host galaxy component since such a component cannot be well constrained for most of our objects at $z \gtrsim 1$. Empirical corrections for host starlight for the low-z subset of our quasars are discussed in Section 3.3.

The continuum and Fe II emission models are given by the following equations:

$$f_{\rm pl}(\lambda) = a_0(\lambda/\lambda_0)^{a_1}, \quad (1)$$

$$f_{\rm poly}(\lambda) = \sum_{i=1}^{3} b_i(\lambda - \lambda_0)^i, \quad (2)$$

$$f_{\rm Fe\,II}(\lambda) = c_0 F_{\rm Fe\,II}(\lambda, c_1, c_2), \quad (3)$$

$$f_{\rm conti}(\lambda) = f_{\rm pl} + f_{\rm poly} + f_{\rm Fe\,II}, \quad (4)$$

where $\lambda_0 = 3000$ Å is the reference wavelength, and a_i, b_i, and c_i are the model parameters; specifically, c_1 and c_2 are the Gaussian broadening and wavelength shift parameters applied to the Fe II templates to match the data.

We then fit the line spectrum in logarithmic wavelength space, i.e., the natural binning scheme of SDSS spectra. The fitting is performed on individual line complexes where multiple lines are close in wavelength. Table 1 lists the detailed information of line complexes and the fitting parameters. In each line complex, we fit a set of Gaussians to individual lines, with constraints on their velocities and widths. We generally do not constrain the flux ratio of line doublets, but we fix the flux ratio[23] of the [S II] $\lambda\lambda$6717, 6731 doublet to be 1 and the flux ratio of the [N II] $\lambda\lambda$6548, 6584 doublet to be $f_{6584}/f_{6548} = 3$. For most permitted lines, we attempt to decompose the narrow-line component and the broad-line component. However, for weak lines and lines that lack a distinctive division between broad and narrow lines (such as C IV), we do not attempt such a decomposition. Figure 2 shows an example of our model fit for quality assessment (QA); the full set of QA plots are available on the SDSS-RM data server and on Zenodo [doi:10.5281/zenodo.2565390].

Many high-z quasars have UV absorption lines imprinted on the spectrum, which may bias the continuum and emission-line fits. To remedy the effect of absorption lines, in the fit, we mask pixels that are 5σ below the 20 pixel boxcar smoothed spectrum. In addition, we perform one iteration after rejecting pixels that fall 3σ below the previous fit. The combination of these two absorption rejection criteria is a good recipe for correcting the effects of narrow absorption lines (NALs) and somewhat improves the fits for broad absorption-line quasars.

We measure continuum luminosities and emission-line properties (line peak, FWHM, equivalent width, etc.) from the model fits to the spectrum. These spectral properties are compiled in the main catalog described in Table 2. In addition to the primary broad and narrow emission lines, we include measurements for the narrow [O II] λ3728 and [Ne V] λ3426 lines and the stellar absorption line Ca II λ3934 (K). As discussed in Shen et al. (2016a), these relatively isolated lines often suffer from imperfect global continuum subtraction. Hence we refit these lines with a local continuum model and report the measurements in Table 2.

To estimate the measurement uncertainties of the spectral properties, we use a Monte Carlo approach: we add to the original spectral flux at each pixel a random Gaussian variate with a zero mean and σ given by the reported error at that pixel and repeat the fitting procedure on the mock spectrum. We create 50 trials and estimate the measurement uncertainty of each spectral quantity (e.g., continuum flux, line FWHM, etc.) as the semi-amplitude of the range enclosing the 16th and 84th percentiles of the distribution from the trials. Adding flux perturbations to the original spectrum instead of the model spectrum preserves details in the spectral features (such as absorption lines) that are not captured or well-fit by our model. On the other hand, the original spectrum is already a perturbed version of the noise-free true spectrum, hence the mock spectra are slightly noisier than the original spectrum, and, therefore,

Table 1
Line Fitting Parameters

Line Complex (1)	Fitting Range (Å) (2)	Line (3)	$n_{\rm Gauss}$ (4)
Hα	6400–6800	Broad Hα	3
		Narrow Hα	1
		[N II]6549	1
		[N II]6585	1
		[S II]6718	1
		[S II]6732	1
Hβ	4640–5100	Broad Hβ	3
		Narrow Hβ	1
		[O III]4959 core	1
		[O III]5007 core	1
		[O III]4959 wing	1
		[O III]5007 wing	1
		Broad He II 4687	1
		Narrow He II 4687	1
Mg II	2700–2900	Broad Mg II	2
		Narrow Mg II	1
C III]	1700–1970	C III]	2
		Si III] 1892	1
		Al III 1857	1
		[Si II] 1816	1
		N III 1750	1
		N IV 1718	1
C IV	1500–1700	C IV	3
		Broad He II 1640	1
		Narrow He II 1640	1
		Broad O III 1663	1
		Narrow O III 1663	1
Si IV	1290–1450	Broad Si IV/O IV]	2
		C II 1335	1
		O I 1304	1
Lyα	1150–1290	Lyα	3
		N V 1240	1

Note. Our emission-line fits are performed in individual line complexes, where multiple lines are fit simultaneously. The last column lists the number of Gaussians used for each line.

[23] We fix the flux ratio for [S II] $\lambda\lambda$6717, 6731 because the lines are weak; we fix the flux ratio for [N II] $\lambda\lambda$6548, 6584 to reduce ambiguity of line decomposition under the Hα profile.

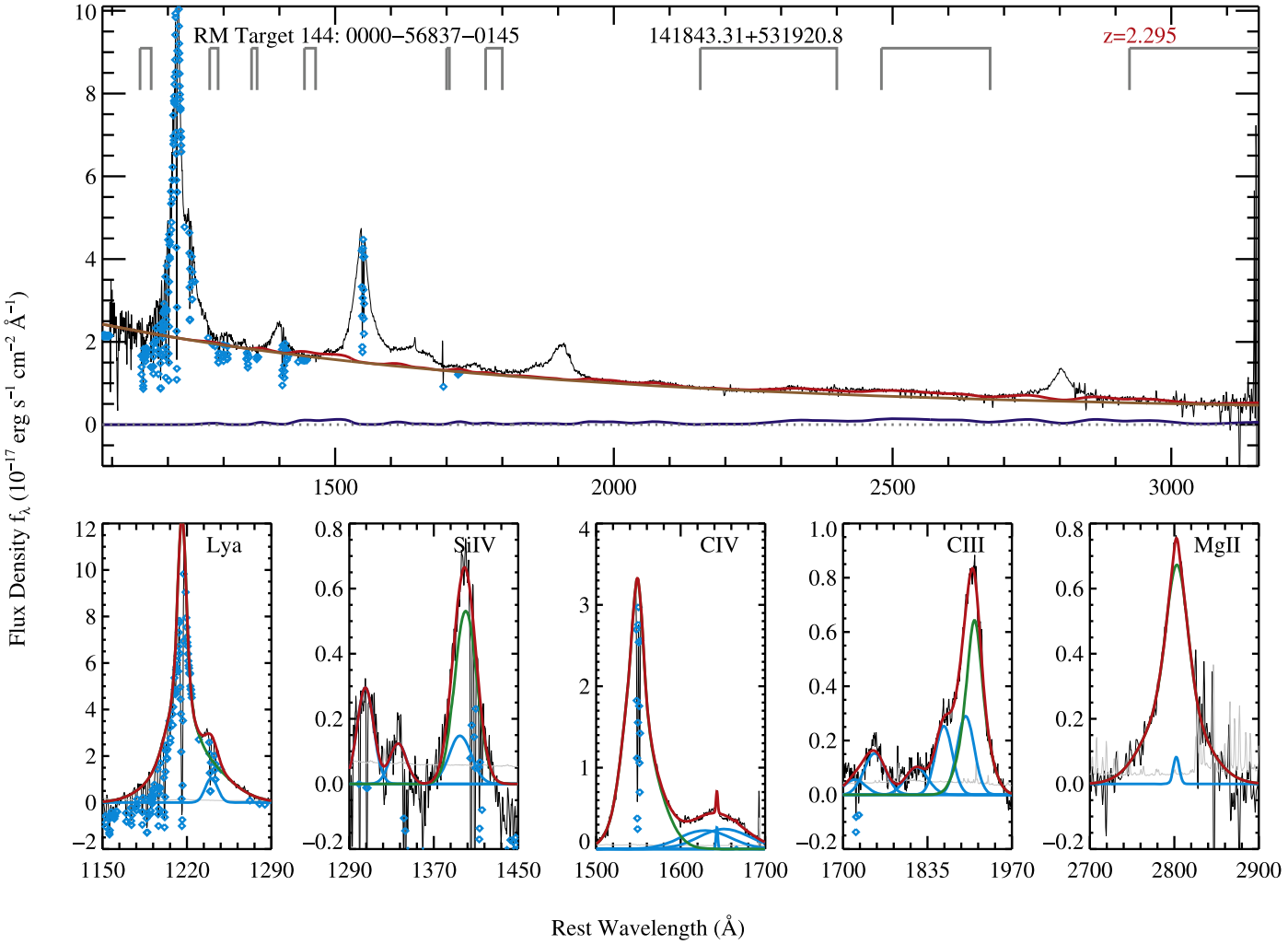

Figure 2. Example of our global spectral fitting approach. The top panel shows the continuum (brown) and Fe II (blue) model components; the red line is the sum of the two. The cyan diamonds are pixels masked as absorption or bad pixels. The gray brackets near the top of the panel indicate the windows used for the continuum +Fe II fit. The bottom panels present the emission-line fits for five line complexes.

our approach will produce more conservative measurement errors in the spectral quantities.

Additional information about the global fitting code is provided in the Appendix.

3.2. S/N Dependence

The high S/N of the coadded spectra also allows investigation of the S/N dependence of our spectral measurements. Similar analyses were performed to evaluate the robustness of the measured line peaks in Shen et al. (2016a) and C IV line widths in Denney et al. (2016b); here, we extend this exercise to a more complete list of lines and spectral quantities. We degrade the original high-S/N spectra by inflating the original flux errors by a constant scaling factor and by perturbing the spectrum using the new errors. We then perform the same fitting procedure on the degraded spectra and compare the results with those based on the original high-S/N spectra. This approach isolates the effect of an S/N from that of the intrinsic variability of the quasar on the spectral measurements, but still explores the full range of spectral diversity.

We already demonstrated in Shen et al. (2016a) that the peak wavelengths of the lines can be measured reasonably well even if the median S/N of the spectrum is as low as ∼3 per SDSS pixel, with negligible biases (e.g., Figure 3 of Shen et al. 2016a). Figure 3 shows the difference (normalized by measurement uncertainties) between measurements from the degraded spectra and from the high-S/N coadded spectra for typical narrow and broad lines of quasars for the line FWHMs (top panel) and rest-frame equivalent widths (REW, bottom panel). As with the case of line peaks, there is no systematic bias in the measurements when the spectral S/N is degraded to as low as ∼3 per SDSS pixel, which is consistent with our earlier findings using general SDSS quasars (Shen et al. 2011). This comparison also demonstrates that our measurement errors estimated from the Monte Carlo approach are reasonable (or even more conservative) because they yield normalized distributions consistent with the expected Gaussian distribution with unity dispersion.

It is also interesting to note that the FWHM of the C IV line, which often displays asymmetric and blueshifted profiles, can be measured robustly with the multi-Gaussian function even at an S/N of a few with negligible bias. This result differs from

Table 2
FITS Catalog Format

Column	Format	Units	Description
RMID	LONG		Object ID of SDSS-RM quasars
RA	DOUBLE	degree	J2000 RA
DEC	DOUBLE	degree	J2000 DEC
ZPIP	DOUBLE		Pipeline redshift
ZSYS	DOUBLE		Improved systemic redshift
ZSYS_ERR	DOUBLE		Uncertainty in systemic redshift (systematic and statistical combined)
PSFMAG	DOUBLE[5]	mag	SDSS PSF magnitudes in $(ugriz)_{\rm SDSS}$; undereddened for Galactic extinction
MI	DOUBLE	mag	Absolute i-band magnitude; undereddened for Galactic extinction
MI_Z2	DOUBLE	mag	K-corrected absolute i-band magnitude (normalized at $z = 2$)
BOSS_TARGET1	LONG64		SDSS-III BOSS target bits
BOSS_TARGET2	LONG64		SDSS-III BOSS target bits
ANCILLARY_TARGET1	LONG64		SDSS-III BOSS ancillary target bits
ANCILLARY_TARGET2	LONG64		SDSS-III BOSS ancillary target bits
PRIMTARGET	LONG64		SDSS-I/II DR7 primary target bits
SECTAEGET	LONG64		SDSS-I/II DR7 secondary target bits
OTHER_TARGET	STRING		Other target flags
PLATE_ALL	STRING		Plate list of previous SDSS spectra (before SDSS-RM)
FIBER_ALL	STRING		Fiber list of previous SDSS spectra (before SDSS-RM)
MJD_ALL	STRING		MJD list of previous SDSS spectra (before SDSS-RM)
PS1_NMAG_OK	LONG[5]		Number of good PS1 epochs in $(grizY)_{\rm PS1}$
PS1_RMS_MAG	DOUBLE[5]	mag	Intrinsic rms magnitude of the PS1 light curves in $(grizY)_{\rm PS1}$ (PSF mag)
ALLWISE1234	DOUBLE[4]	mag	*WISE* magnitudes from the ALLWISE release
ALLWISE1234_ERR	DOUBLE[4]	mag	Uncertainties in ALLWISE magnitudes
ALLWISE_OFFSET	DOUBLE	arcsec	Angular separation between SDSS and ALLWISE matches
UNWISE1234	DOUBLE[4]	mag	Forced unWISE photometry at the SDSS position from Lang et al. (2016)
UNWISE1234_ERR	DOUBLE[4]	mag	Uncertainties in unWISE magnitudes
BAL_FLAG	LONG		Broad absorption-line flag; 0 = nonBAL or no coverage; 1 = HiBAL; 2 = LoBAL; 3 = FeLoBAL
NABS	LONG		Number of narrow absorption-line systems
ZABS	DOUBLE[10]		Absorber redshifts of narrow absorption-line systems (maximum 10)
FIRST_FR_TYPE	LONG		FIRST radio morphology type; −1 = not in FIRST footprint; 0 = FIRST undetected; 1 = core-dominant; 2 = lobe-dominant
FIRST_FINT_MJY	DOUBLE	mJy	FIRST integrated flux density at 20 cm
FINT_REST6CM_MJY_OBS	DOUBLE	mJy	Observed radio flux density at rest-frame 6 cm
LOGFNU2500A_ERGS_OBS	DOUBLE	erg s^{-1} cm^{-2} Hz^{-1}	Observed optical flux density at rest-frame 2500 Å
R_6CM_2500A	DOUBLE		Radio loudness $R \equiv f_{\nu,6\,\rm cm}/f_{\nu,2500\,\text{Å}}$
F_H_5100	DOUBLE		Host fraction at rest-frame 5100 Å from Shen et al. (2015b)
SIGMA	DOUBLE	km s^{-1}	Host stellar velocity dispersion from Shen et al. (2015b)
SIGMA_ERR	DOUBLE	km s^{-1}	Uncertainty in SIGMA
SIGMA_ERR_WARNING	LONG		1 if SIGMA_ERR may underestimate the systematic uncertainty
CONTI_FIT	DOUBLE[14]		Best-fit parameters for the continuum model
CONTI_FIT_ERR	DOUBLE[14]		Uncertainties in the best-fit continuum parameters
CONTI_REDCHI2	DOUBLE		Reduced χ^2 for the continuum fit
FEII_UV	DOUBLE[3]		Best-fit parameters for the UV Fe II model
FEII_UV_ERR	DOUBLE[3]		Uncertainties in the best-fit UV Fe II model
FEII_OPT	DOUBLE[3]		Best-fit parameters for the optical Fe II model
FEII_OPT_ERR	DOUBLE[3]		Uncertainties in the best-fit optical Fe IImodel
LOGL1350	DOUBLE	[erg s^{-1}]	Continuum luminosity at rest-frame 1350 Å
LOGL1350_ERR	DOUBLE	[erg s^{-1}]	Uncertainty in LOGL1350
LOGL1700	DOUBLE	[erg s^{-1}]	Continuum luminosity at rest-frame 1700 Å
LOGL1700_ERR	DOUBLE	[erg s^{-1}]	Uncertainty in LOGL1700
LOGL3000	DOUBLE	[erg s^{-1}]	Continuum luminosity at rest-frame 3000 Å
LOGL3000_ERR	DOUBLE	[erg s^{-1}]	Uncertainty in LOGL3000
LOGL5100	DOUBLE	[erg s^{-1}]	Continuum luminosity at rest-frame 5100 Å
LOGL5100_ERR	DOUBLE	[erg s^{-1}]	Uncertainty in LOGL5100
LOGLBOL	DOUBLE	[erg s^{-1}]	Bolometric luminosity
LOGLBOL_ERR	DOUBLE	[erg s^{-1}]	Uncertainty in LOGLBOL
REW_FE_4434_4684	DOUBLE	Å	Rest-frame equivalent width of optical Fe II within 4434–4684 Å
REW_FE_4434_4684_ERR	DOUBLE	Å	Uncertainty in REW_FE_4434_4684
REW_FE_2250_2650	DOUBLE	Å	Rest-frame equivalent width of UV Fe II within 2250–2650 Å
REW_FE_2250_2650_ERR	DOUBLE	Å	Uncertainty in REW_FE_2250_2650
SII6718	DOUBLE[5]	Å, km s^{-1}, [erg s^{-1}], Å, Å	peak wavelength, FWHM, $\log L_{\rm line}$, rest-frame EW, top 50% flux centroid

Table 2
(Continued)

Column	Format	Units	Description
HALPHA	DOUBLE[5]	...	For the entire Hα profile (narrow and broad lines combined)
HALPHA_BR	DOUBLE[5]	...	For the broad Hα component
NII6585	DOUBLE[5]	...	For the narrow [N II] λ6584 component
HBETA	DOUBLE[5]	...	For the entire Hβ profile (narrow and broad lines combined)
HBETA_BR	DOUBLE[5]	...	For the broad Hβ component
HEII4687	DOUBLE[5]	...	For the entire He II λ4687 profile (narrow and broad lines combined)
HEII4687_BR	DOUBLE[5]	...	For the broad He II λ4687 component
OIII5007	DOUBLE[5]	...	For the entire [O III] λ5007 profile
OIII5007C	DOUBLE[5]	...	For the core [O III] λ5007 profile
CAII3934	DOUBLE[5]	...	For the Ca II K absorption line
OII3728	DOUBLE[5]	...	...
NEV3426	DOUBLE[5]	...	...
MGII	DOUBLE[5]	...	For the entire Mg II profile (narrow and broad lines combined)
MGII_BR	DOUBLE[5]	...	For the broad Mg II component
CIII_ALL	DOUBLE[5]	...	For the entire C III] complex (C III], Si III], Al III)
CIII_BR	DOUBLE[5]	...	For the broad C III] component
SIIII1892	DOUBLE[5]	...	...
ALIII1857	DOUBLE[5]	...	...
NIII1750	DOUBLE[5]	...	...
CIV	DOUBLE[5]	...	...
HEII1640	DOUBLE[5]	...	For the entire He II λ1640 profile (narrow and broad lines combined)
HEII1640_BR	DOUBLE[5]	...	For the broad He II λ1640 component
SIIV_OIV	DOUBLE[5]	...	For the 1400 Å complex
OI1304	DOUBLE[5]	...	...
LYA	DOUBLE[5]	...	...
NV1240	DOUBLE[5]	...	...
SII6718_ERR	DOUBLE[5]	Å, km s^{-1}, [erg s^{-1}], Å, Å	Measurement errors in [S II] λ6717
HALPHA_ERR	DOUBLE[5]	...	...
HALPHA_BR_ERR	DOUBLE[5]	...	...
NII6585_ERR	DOUBLE[5]	...	...
HBETA_ERR	DOUBLE[5]	...	...
HBETA_BR_ERR	DOUBLE[5]	...	...
HEII4687_ERR	DOUBLE[5]	...	...
HEII4687_BR_ERR	DOUBLE[5]	...	...
OIII5007_ERR	DOUBLE[5]	...	...
OIII5007C_ERR	DOUBLE[5]	...	...
CAII3934_ERR	DOUBLE[5]	...	...
OII3728_ERR	DOUBLE[5]	...	...
NEV3426_ERR	DOUBLE[5]	...	...
MGII_ERR	DOUBLE[5]	...	...
MGII_BR_ERR	DOUBLE[5]	...	...
CIII_ALL_ERR	DOUBLE[5]	...	...
CIII_BR_ERR	DOUBLE[5]	...	...
SIIII1892_ERR	DOUBLE[5]	...	...
ALIII1857_ERR	DOUBLE[5]	...	...
NIII1750_ERR	DOUBLE[5]	...	...
CIV_ERR	DOUBLE[5]	...	...
HEII1640_ERR	DOUBLE[5]	...	...
HEII1640_BR_ERR	DOUBLE[5]	...	...
SIIV_OIV_ERR	DOUBLE[5]	...	...
OI1304_ERR	DOUBLE[5]	...	...
LYA_ERR	DOUBLE[5]	...	...
NV1240_ERR	DOUBLE[5]	...	...
LOGBH_CIV_VP06	DOUBLE	[$M_\odot$]	Single-epoch BH mass based on C IV (Vestergaard & Peterson 2006)
LOGBH_CIV_VP06_ERR	DOUBLE	...	...
LOGBH_MGII_S11	DOUBLE	...	Single-epoch BH mass based on Mg II (Shen et al. 2011)
LOGBH_MGII_S11_ERR	DOUBLE	...	...
LOGBH_HB_VP06	DOUBLE	...	Single-epoch BH mass based on Hβ (Vestergaard & Peterson 2006)
LOGBH_HB_VP06_ERR	DOUBLE	...	...
LOGBH	DOUBLE	...	Fiducial single-epoch BH mass
LOGBH_ERR	DOUBLE	...	
LOGEDD_RATIO	DOUBLE	...	Eddington ratio based on fiducial single-epoch BH mass
LOGEDD_RATIO_ERR	DOUBLE		
RMS_ML_C1700	DOUBLE	erg s^{-1} cm^{-2} Å^{-1}	(Maximum-likelihood) rms variability for rest 1700 Å continuum

Table 2
(Continued)

Column	Format	Units	Description
RMS_ML_C1700_ERR	DOUBLE	erg s^{-1} cm^{-2} $Å^{-1}$	
SNR_RMS_ML_C1700	DOUBLE		RMS_ML_C1700/RMS_ML_C1700_ERR
RMS_ML_FRAC_C1700	DOUBLE		Fractional (with respect to average) rms variability for rest 1700 Å continuum
RMS_ML_FRAC_C1700_ERR	DOUBLE		
N_RMS_GOOD_C1700	FLOAT		Effective number of good data points in estimating RMS_ML_C1700
SNR2_C1700	DOUBLE		Alternative measure of the variability for rest 1700 Å continuum
RMS_ML_C3000	DOUBLE	erg s^{-1} cm^{-2} $Å^{-1}$	(Maximum-likelihood) rms variability for rest 3000 Å continuum
RMS_ML_C3000_ERR	DOUBLE	erg s^{-1} cm^{-2} $Å^{-1}$	
SNR_RMS_ML_C3000	DOUBLE		RMS_ML_C3000/RMS_ML_C3000_ERR
RMS_ML_FRAC_C3000	DOUBLE		Fractional (with respect to average) rms variability for rest 3000 Å continuum
RMS_ML_FRAC_C3000_ERR	DOUBLE		
N_RMS_GOOD_C3000	FLOAT		Effective number of good data points in estimating RMS_ML_C3000
SNR2_C3000	DOUBLE		Alternative measure of the variability for rest 3000 Å continuum
RMS_ML_C5100	DOUBLE	erg s^{-1} cm^{-2} $Å^{-1}$	(Maximum-likelihood) rms variability for rest 5100 Å continuum
RMS_ML_C5100_ERR	DOUBLE	erg s^{-1} cm^{-2} $Å^{-1}$	
SNR_RMS_ML_C5100	DOUBLE		RMS_ML_C5100/RMS_ML_C5100_ERR
RMS_ML_FRAC_C5100	DOUBLE		Fractional (with respect to average) rms variability for rest 5100 Å continuum
RMS_ML_FRAC_C5100_ERR	DOUBLE		
N_RMS_GOOD_C5100	FLOAT		Effective number of good data points in estimating RMS_ML_C5100
SNR2_C5100	DOUBLE		Alternative measure of the variability for rest 5100 Å continuum
RMS_ML_HA	DOUBLE	erg s^{-1} cm^{-2}	(Maximum-likelihood) rms variability for broad Hα
RMS_ML_HA_ERR	DOUBLE	erg s^{-1} cm^{-2}	
SNR_RMS_ML_HA	DOUBLE		RMS_ML_HA/RMS_ML_HA_ERR
RMS_ML_FRAC_HA	DOUBLE		Fractional (with respect to average) rms variability for broad Hα
RMS_ML_FRAC_HA_ERR	DOUBLE		
N_RMS_GOOD_HA	FLOAT		Effective number of good data points in estimating RMS_ML_HA
SNR2_HA	DOUBLE		Alternative measure of the variability for broad Hα
RMS_ML_HB	DOUBLE	erg s^{-1} cm^{-2}	(Maximum-likelihood) rms variability for broad Hβ
RMS_ML_HB_ERR	DOUBLE	erg s^{-1} cm^{-2}	
SNR_RMS_ML_HB	DOUBLE		RMS_ML_HB/RMS_ML_HB_ERR
RMS_ML_FRAC_HB	DOUBLE		Fractional (with respect to average) rms variability for broad Hβ
RMS_ML_FRAC_HB_ERR	DOUBLE		
N_RMS_GOOD_HB	FLOAT		Effective number of good data points in estimating RMS_ML_HB
SNR2_HB	DOUBLE		Alternative measure of the variability for broad He II 4687
RMS_ML_HEII4687	DOUBLE	erg s^{-1} cm^{-2}	(Maximum-likelihood) rms variability for broad He II 4687
RMS_ML_HEII4687_ERR	DOUBLE	erg s^{-1} cm^{-2}	
SNR_RMS_ML_HEII4687	DOUBLE		RMS_ML_HEII4687/RMS_ML_HEII4687_ERR
RMS_ML_FRAC_HEII4687	DOUBLE		Fractional (with respect to average) rms variability for broad He II 4687
RMS_ML_FRAC_HEII4687_ERR	DOUBLE		
N_RMS_GOOD_HEII4687	FLOAT		Effective number of good data points in estimating RMS_ML_HEII4687
SNR2_HEII4687	DOUBLE		Alternative measure of the variability for broad He II 4687
RMS_ML_MGII	DOUBLE	erg s^{-1} cm^{-2}	(Maximum-likelihood) rms variability for broad Mg II
RMS_ML_MGII_ERR	DOUBLE	erg s^{-1} cm^{-2}	
SNR_RMS_ML_MGII	DOUBLE		RMS_ML_MGII/RMS_ML_MGII_ERR
RMS_ML_FRAC_MGII	DOUBLE		Fractional (with respect to average) rms variability for broad Mg II
RMS_ML_FRAC_MGII_ERR	DOUBLE		
N_RMS_GOOD_MGII	FLOAT		Effective number of good data points in estimating RMS_ML_MGII
SNR2_MGII	DOUBLE		Alternative measure of the variability for broad Mg II
RMS_ML_CIII	DOUBLE	erg s^{-1} cm^{-2}	(Maximum-likelihood) rms variability for the full C III] complex
RMS_ML_CIII_ERR	DOUBLE	erg s^{-1} cm^{-2}	
SNR_RMS_ML_CIII	DOUBLE		RMS_ML_CIII/RMS_ML_CIII_ERR
RMS_ML_FRAC_CIII	DOUBLE		Fractional (with respect to average) rms variability for the full C III] complex
RMS_ML_FRAC_CIII_ERR	DOUBLE		
N_RMS_GOOD_CIII	FLOAT		Effective number of good data points in estimating RMS_ML_CIII
SNR2_CIII	DOUBLE		Alternative measure of the variability for the full C III] complex
RMS_ML_CIV	DOUBLE	erg s^{-1} cm^{-2}	(Maximum-likelihood) rms variability for broad C IV
RMS_ML_CIV_ERR	DOUBLE	erg s^{-1} cm^{-2}	
SNR_RMS_ML_CIV	DOUBLE		RMS_ML_CIV/RMS_ML_CIV_ERR
RMS_ML_FRAC_CIV	DOUBLE		Fractional (with respect to average) rms variability for broad C IV
RMS_ML_FRAC_CIV_ERR	DOUBLE		
N_RMS_GOOD_CIV	FLOAT		Effective number of good data points in estimating RMS_ML_CIV
SNR2_CIV	DOUBLE		Alternative measure of the variability for broad C IV

Table 2
(Continued)

Column	Format	Units	Description
RMS_ML_LYA	DOUBLE	erg s^{-1} cm^{-2}	(Maximum-likelihood) rms variability for broad Lyα
RMS_ML_LYA_ERR	DOUBLE	erg s^{-1} cm^{-2}	
SNR_RMS_ML_LYA	DOUBLE		RMS_ML_LYA/RMS_ML_LYA_ERR
RMS_ML_FRAC_LYA	DOUBLE		Fractional (with respect to average) rms variability for broad Lyα
RMS_ML_FRAC_LYA_ERR	DOUBLE		
N_RMS_GOOD_LYA	FLOAT		Effective number of good data points in estimating RMS_ML_LYA
SNR2_LYA	DOUBLE		Alternative measure of the variability for broad Lyα
COMMENT	STRING	...	Comments on individual objects

Note. (1) *K*-corrections are the same as in Richards et al. (2006b). (2) Bolometric luminosities are computed using bolometric corrections of 9.26, 5.15, and 3.81 (Richards et al. 2006a) using the 5100, 3000, and 1350 Å monochromatic luminosities, respectively, with 3000 Å luminosity being the highest priority. (3) Uncertainties are measurement errors only. (4) Unless otherwise stated, unmeasurable values are indicated with zero for a quantity and −1 for its associated error, except for LOGEDD_RATIO where the unmeasurable values are −99. (5) In general, the FWHM of the total line profile is smaller than that of the broad-only component. However, in cases where the narrow and broad components are significantly offset in velocity (e.g., He II 1640 in some objects), the total line FWHM can be larger than the broad-line-only FWHM.

the case where a Gauss–Hermite function (e.g., van der Marel & Franx 1993) is used instead to fit the C IV line, where a systematic bias with respect to the S/N is observed (e.g., Denney et al. 2016b). As discussed in that paper, this behavior is due to the fact that the Gauss–Hermite model is more flexible than the multi-Gaussian model and tends to over-fit the line when the S/N is low, leading to a systematic bias in the FWHM measurement. On the other hand, we adopted a three-Gaussian model for the C IV line in this work, as opposed to the two-Gaussian model used for the comparison in Denney et al. (2016b). For high-S/N spectra, the three-Gaussian model reproduces the C IV line profile better than a two-Gaussian model and just as well as the Gauss–Hermite model, but does not have a systematic bias as the S/N decreases as for the Gauss–Hermite model (Denney et al. 2016b). Based on these results, we conclude that the multi-Gaussian model is a better function to use for the C IV line in general than the Gauss–Hermite model, particularly for survey-quality spectra.

While we focused on the general quasar population and concluded that S/N degradation does not lead to significant biases in the spectral measurements, it is possible that certain individual objects with peculiar line profiles are more sensitive to S/N degradation, which, of course, also depends on the flexibility of the fitting model.

3.3. Host Galaxy Properties

For low-redshift ($z \lesssim 1$) objects in the SDSS-RM sample, there could be significant host contamination in the continuum. We used a spectral decomposition technique described in Vanden Berk et al. (2006) and Shen et al. (2008a) to decompose the spectrum into quasar and host galaxy components. Shen et al. (2015b) provided details on the application of this spectral decomposition to the SDSS-RM quasar sample and presented successful decomposition and measurements of the host stellar velocity dispersion in ∼100 SDSS-RM quasars at $z \lesssim 1.1$. Consistent results were obtained with independent spectral decomposition in Matsuoka et al. (2015) and with imaging decomposition in Yue et al. (2018) for the same SDSS-RM sample. For convenience, we have compiled the host fraction at 5100 Å and stellar velocity dispersion measurements from Shen et al. (2015b) in the main catalog presented here.

3.4. Improved Redshifts

With the measured line peaks from our spectral fits, we improve the systemic redshift estimation of SDSS-RM quasars following the recipes in Shen et al. (2016a). In short, Shen et al. (2016a) recommended a ranked list of lines as redshift indicators using the measured line peak, calibrated to be consistent with those derived from the stellar absorption lines on average. We adopt the line-based redshift with the smallest combined systematic and measurement uncertainty as the systemic redshift.

Figure 4 presents the comparison of the median composite spectra generated by coadding all SDSS-RM quasars with the pipeline redshifts and the improved systemic redshifts, following the methodology of generating composite spectrum in Vanden Berk et al. (2001). The lines in the composite spectrum with the improved redshifts are significantly sharper, and are better aligned with the Ca II λ3934 velocity, than those in the composite spectrum with the pipeline redshifts, indicating that our revised redshifts are more accurate than the pipeline redshifts. Most quasar emission lines, on average, have an intrinsic offset velocity from the systemic velocity based on stellar absorption lines, as determined in Shen et al. (2016a). These average velocity offsets are reflected in the composite spectrum shown in Figure 4.

3.5. Absorption-line Systems

A significant fraction of high-z quasars in the SDSS-RM sample show broad and/or NALs in their spectra. We have identified these absorption-line systems with independent approaches from our spectral fitting described above. These absorption-line systems can be used to study the time variability of absorption using spectra from individual epochs, as well as detailed abundance of the narrow absorbers with the coadded high-S/N spectra. Some initial results on the time variability of broad absorption troughs were reported in Grier et al. (2015) and Hemler et al. (2019).

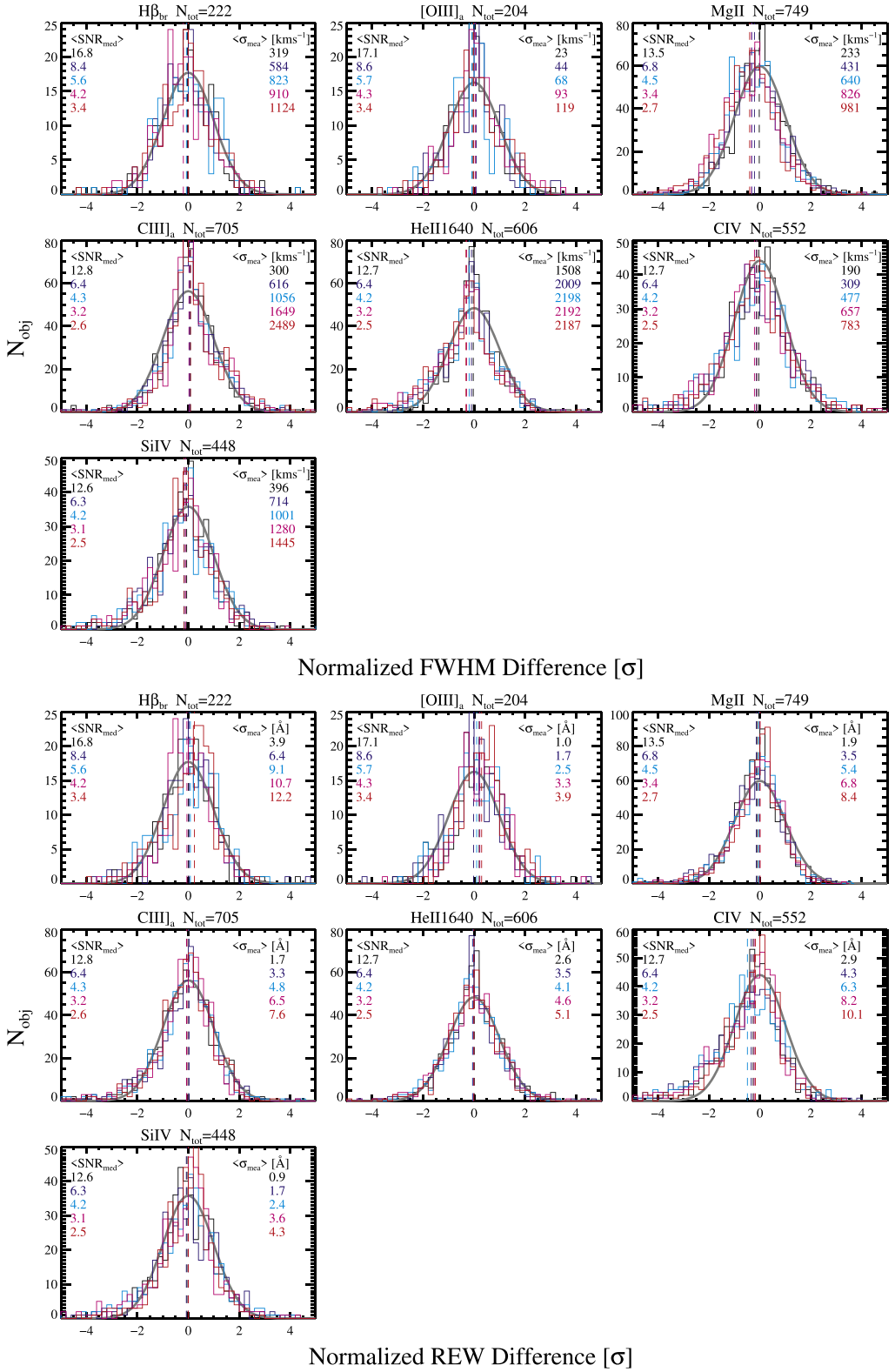

Figure 3. Distribution of the difference in the measured line FWHM (top panel) and rest EW (bottom panel) between the original high-S/N spectra and the degraded spectra, normalized by the measurement uncertainty (the quadrature sum of the measurement uncertainties in both measurements). Each panel shows results for a specific line, with the total number of objects listed at the top. Different colors represent different degradations of the original S/N by a factor of 2, 4, 6, 8, and 10. The sample median of the median S/N across the spectral range ($\langle \mathrm{SNR_{med}} \rangle$) and the sample median measurement uncertainty ($\langle \sigma \rangle_{\mathrm{mea}}$) in the degraded spectra are marked in each panel. The median of the distribution is indicated by the vertical dashed line. The gray solid line is a Gaussian with a zero mean and unity dispersion, normalized to have the same area as the observed distribution. For all lines and all cases of S/N degradation, there is a negligible offset in the distribution, indicating that the measurement of line peak is unbiased when the continuum S/N is decreased to as low as ∼3 per SDSS pixel. In addition, the agreement between the observed distributions and the unity Gaussian suggests that our estimated measurement uncertainties from the Monte Carlo approach are reasonable.

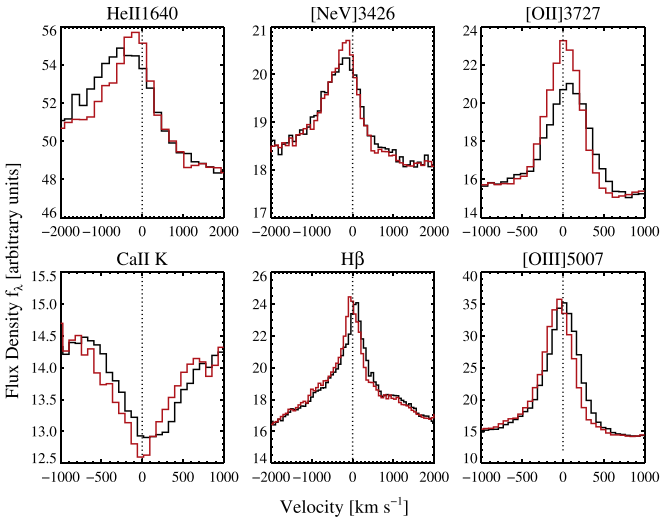

Figure 4. Median composite spectra around several emission/stellar absorption lines of the SDSS-RM sample, generated using the pipeline redshifts (black lines) and the improved systemic redshift (red lines). The systemic redshifts make the line features in the composite spectrum sharper or closer to the expected wavelengths.

3.5.1. BALQSOs

We identify 95 quasars with broad absorption-line (BAL) troughs based on the 2014 spectra.

BAL and mini-BAL quasars (e.g., Trump et al. 2006; Gibson et al. 2009; Pâris et al. 2017) were identified by their absorption troughs. Troughs were visually identified by inspecting coadded spectra from the first year of observations (2014). No limits were placed on the velocity of the absorption relative to the quasar's systemic redshift. BALs were searched for in C IV, Al III, Mg II, Fe II, and Fe III.

A maximum trough velocity width for each BAL quasar was estimated using the widest trough in the 2014 coadded spectrum (whenever possible). Velocity limits were set where the trough reached 90% of the estimated unabsorbed continuum. That raw width was corrected to a true velocity width of the absorbing gas by subtracting the velocity separation of the doublet involved (C IV or Mg II).

We adopt the convention that BAL quasars have troughs $>2000\,\mathrm{km\,s^{-1}}$ wide and that mini-BAL quasars (e.g., Rodríguez Hidalgo et al. 2011) have troughs that are 500–2000 $\mathrm{km\,s^{-1}}$ wide. No troughs $<500\,\mathrm{km\,s^{-1}}$ wide were selected for our sample, and we neither include apparent mini-BAL troughs that are collections of narrow C IV absorbers clustered in velocity space (as revealed by narrow absorption in other ions, such as N V or Si IV). Therefore, from the perspective of automated identification of troughs in a certain range of velocity widths, our sample is incomplete. From the perspective of studying broad intrinsic absorption, our sample should be highly complete: we rejected half a dozen borderline mini-BAL candidates.

We classify these BALQSOs into three classes: (1) HiBAL (72 quasars): quasars with C IV BAL toughs only; (2) LoBAL (21 quasars): quasars with both C IV and Mg II/Al III BALs; and (3) FeLoBAL (2 quasars): LoBAL quasars with additional Fe BAL troughs. Some HiBAL quasars may have LoBALs that were shifted out of the SDSS spectral coverage.

We provide the list of 95 BAL quasars and notes on individual objects in a CSV file on Zenodo [doi:10.5281/zenodo.2565390], which is also distributed in the SDSS-RM data server.

3.5.2. Narrow Absorbers

We have identified NALs imprinted on the SDSS-RM quasar spectra following the approach described in detail in Zhu & Ménard (2013). The search for NALs was limited to 10 absorption systems per sight-line at different absorber redshifts, since the vast majority of SDSS-RM quasars have fewer NAL systems. To reduce the impact of broad absorption lines in high-ionization lines such as C IV, which will make the identification of NALs difficult, we focus the search on Mg II absorption-line systems and associated lines (e.g., Fe II). Given the much higher S/N in the coadded SDSS-RM spectra than regular SDSS spectra, we were able to identify weaker absorption-line systems than those reported in Zhu & Ménard (2013).

For each NAL system identified, we measure the absorption EW and dispersion of a list of line species using Gaussian fits (e.g., Zhu & Ménard 2013). Our main catalog compilation in Table 2 provides the redshifts of the identified NAL systems, and detailed measurements of these absorbers are provided in supplemental data files, with the same format as the NAL catalog presented in Zhu & Ménard (2013).

3.6. Example Objects of Special Interest

The high-S/N coadded spectra and the time-resolved individual spectra offer a wide range of applications to understand the physics of quasars and to study interesting individual systems. Figure 5 presents several examples of quasars in the SDSS-RM sample that are of particular interest. These include peculiar dust-reddened quasars, quasars with double-peaked broad emission lines (dubbed "disk emitters"; Chen et al. 1989; Eracleous & Halpern 1994), BAL and NAL quasars, strong Fe II emitters, and quasars with unusually strong nitrogen emission (Jiang et al. 2008a).

4. Optical Variability Characterization

The primary goal of SDSS-RM is to detect lags between the continuum and the broad-line flux. Therefore, the optical variability characteristics of our sample are of critical importance. We compute the intrinsic rms magnitudes of SDSS-RM quasars using the early photometric light curves from PS1 during 2010–2013 in five bands ($grizY_{\rm PS1}$; Tonry et al. 2012b) for the MD07 field. Details of photometric calibration are described in Schlafly et al. (2012) and Magnier et al. (2013). The intrinsic rms magnitudes were computed following the approach in Sesar et al. (2007, Equation (6)) and by subtracting the contribution from photometric errors. These (intrinsic) rms magnitudes mostly measure the continuum variability level for our sample over a timescale of 4 yr in the observed frame. Figure 6 shows the distribution of SDSS-RM quasars in the redshift–rms mag plane (for $g_{\rm PS1}$ and $i_{\rm PS1}$; both are PSF magnitudes). The median rms magnitude for SDSS-RM quasars is 0.15 mag in $g_{\rm PS1}$ and 0.11 mag in $i_{\rm PS1}$, which are typical of normal quasars (e.g., Sesar et al. 2007; MacLeod et al. 2010).

We further measure the spectral variability levels using the first-year spectroscopic observations. As detailed in Shen et al. (2016b), PrepSpec fits a model that includes intrinsic variations in the continuum and broad emission lines to the time-resolved spectra and outputs the light curves for continuum and broad-line emission. It also outputs the rms spectrum computed from all spectroscopic epochs. During the PrepSpec fits, an

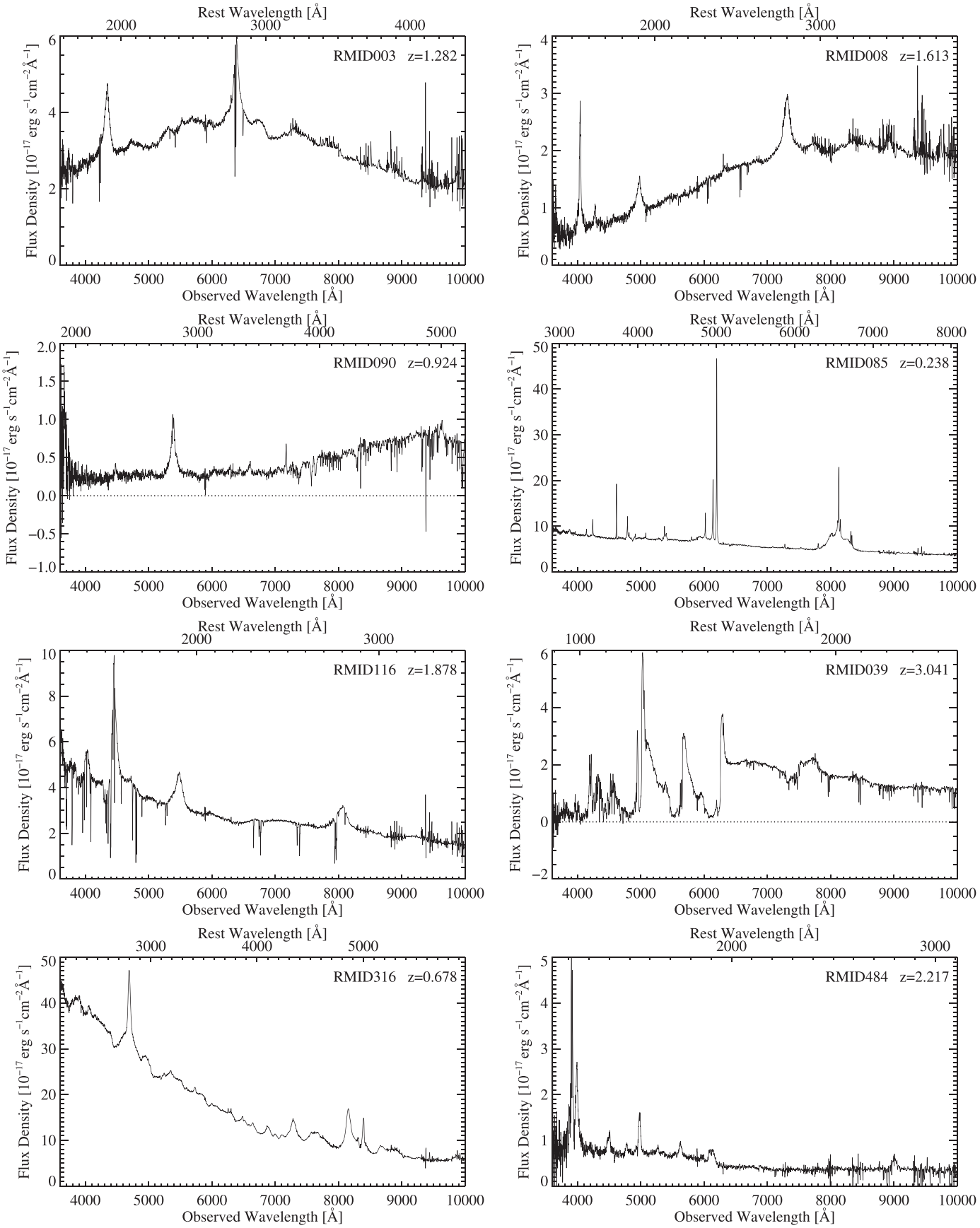

Figure 5. Objects in the SDSS-RM sample that are of particular interest. First row: two quasars with peculiar continuum shapes likely caused by peculiar intrinsic reddening; second row: a quasar with strong stellar absorption lines in rest-frame optical and broad rest-frame UV lines (left), and a quasar showing double-peaked broad Balmer lines (dubbed "disk emitters"; right); third row: a quasar showing many narrow absorption lines (left), and a broad absorption-line quasar (right); and fourth row: an Fe II-rich quasar (left), and a nitrogen-rich quasar (right; e.g., Jiang et al. 2008b; Liu et al. 2018).

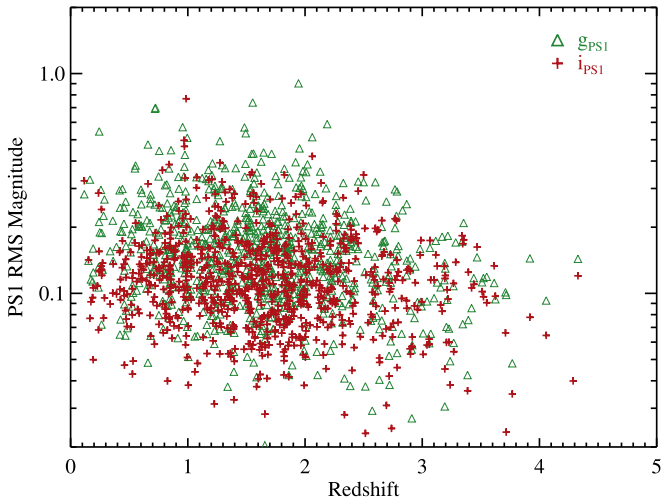

Figure 6. Intrinsic rms magnitudes computed from the PS1 light curves during 2010–2013. We have corrected for photometric errors following the approach of Sesar et al. (2007). These rms magnitudes are typical of quasar continuum variability (e.g., Sesar et al. 2007; MacLeod et al. 2010).

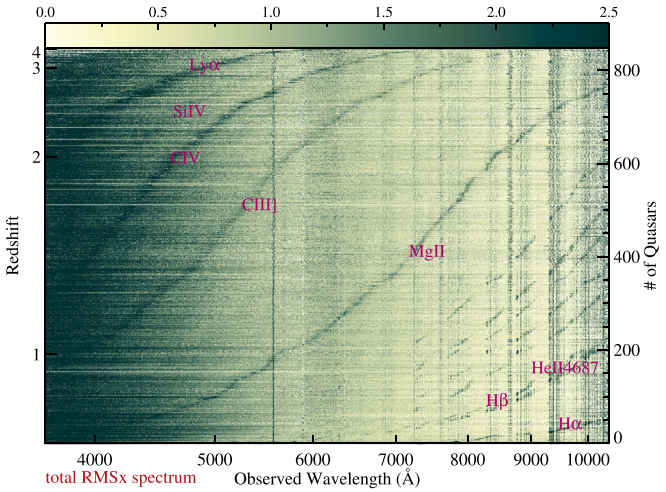

Figure 7. Intrinsic rms spectra based on 2014 data for the 849 SDSS-RM quasars output by PrepSpec and ordered by redshift. Individual rms spectra have been normalized to have a median value of 1. Variability in major broad emission lines are visible as trails (locally enhanced rms variability), running from bottom left to top right. Residuals around some narrow emission lines are also visible due to imperfect PrepSpec fits, which may be reduced in future PrepSpec versions. Sky line residuals are manifested as vertical lines and become more severe near the red edge of the spectra.

additional improvement was made to the flux calibration using available narrow-line fluxes (assumed to be constant during the monitoring period) in individual epochs.

We use the rms spectra generated by PrepSpec on the 2014 SDSS-RM spectroscopy to construct a map of the spectral variability of SDSS-RM quasars in the wavelength and redshift space in Figure 7. These individual rms spectra were the measurement-error-corrected, maximum-likelihood estimate of the excess variability at each wavelength pixel (see below) and were referred to as the "RMSx" spectra in Shen et al. (2016b). To make this map, we normalize individual rms spectra to have a median value of 1. It is apparent from this map that SDSS-RM quasars show significant variability in their broad emission lines, which is a necessary condition to measure a broad-line time lag with respect to the continuum.

Based on the PrepSpec light curves, we quantify the absolute and fractional (with respect to the average) continuum and broad-line variability for the SDSS-RM sample. We use a maximum-likelihood estimator to measure the excess variance of the light curve, as detailed below.

For a given time series X_i with a measurement error of σ_i and an unknown excess variance of σ_0^2 resulting from intrinsic variability, we have

$$\mathrm{Var}[X_i] = \sigma_0^2 + \sigma_i^2 = \frac{\sigma_0^2}{g_i}, \tag{5}$$

where

$$g_i \equiv \frac{\sigma_0^2}{\sigma_0^2 + \sigma_i^2} = \frac{1}{1 + (\sigma_i/\sigma_0)^2} \tag{6}$$

quantifies the "goodness" of X_i for measuring σ_0^2. g_i varies from 0 for points with $\sigma_i \gg \sigma_0$ to 1 for points with $\sigma_i \ll \sigma_0$. The sum of g_i over all data points then provides a "goodness" of measuring the intrinsic variability using the time series and approaches the total number of data points in the limit of $\sigma_i \ll \sigma_0$. We denote the sum of g_i as N_RMS_GOOD, as in Table 2, which has an upper limit of 32 (i.e., total number of spectroscopic epochs in 2014). The distribution of N_RMS_GOOD for our sample varies among different quantities. For continuum light curves, N_RMS_GOOD is mostly around 31. For emission lines, the median value of N_RMS_GOOD is lower and the dispersion is larger. For example, for broad Hβ, the median N_RMS_GOOD is around 23 and the 16%–84% range is N_RMS_GOOD = 13–29. For the weaker He II 4687 broad line, the median N_RMS_GOOD is around 21 and the 16%–84% range is N_RMS_GOOD = 9–27.

The likelihood function given X_i and a constant model of $\mu \equiv \langle X_i \rangle$ with both measurement errors and intrinsic variance is

$$-2\ln L = \sum_{i=1}^{N} \frac{(X_i - \mu)^2}{\sigma_0^2 + \sigma_i^2} + \sum_{i=1}^{N} \ln(\sigma_0^2 + \sigma_i^2). \tag{7}$$

Minimizing the likelihood function, we obtain an estimate of σ_0 as

$$\hat{\sigma_0}^2 = \frac{\sum (X_i - \mu)^2 g_i^2}{\sum g_i},$$
$$\mathrm{Var}[\sigma_0^2] = \frac{\hat{\sigma_0}^4}{\sum g_i \frac{\sum (X_i - \mu)^2 g_i^3}{\sum (X_i - \mu)^2 g_i^2} - \sum g_i^2/2}. \tag{8}$$

To estimate the value of μ, we use the optimal weights of individual data points based on σ_i and σ_0:

$$\hat{\mu} = \frac{\sum \frac{X_i}{\sigma_0^2 + \sigma_i^2}}{\sum \frac{1}{\sigma_0^2 + \sigma_i^2}} = \frac{\sum X_i g_i}{\sum g_i}, \ \mathrm{Var}[\mu] = \frac{\sigma_0}{\sum g_i}. \tag{9}$$

Equations (8) and (9) are solved iteratively. In Table 2, we denote σ_0 as RMS_ML and its uncertainty as RMS_ML_ERR. One caveat is that the estimates for Var[μ] and Var[σ_0^2] in Equations (8) and (9) neglect the (usually small) covariance between $\hat{\mu}$ and $\hat{\sigma}_0^2$.

To quantify how well the intrinsic variability is measured, we employ two separate metrics. The first metric is the S/N of the measured intrinsic rms (SNR_RMS_ML), defined as RMS_ML/RMS_ML_ERR. This metric may be better at a

low S/N, but it saturates near $\sqrt{2(N-1)} = 7.9$ for $N = 32$, when the S/N is large, since there are only N data points available to estimate the intrinsic variance. Therefore, we define a second metric as SNR2 $= \sqrt{\chi^2 - \mathrm{dof}}$, where χ^2 is relative to the optimal average using measurement errors (σ_i) only and dof is the degree of freedom ($N - 1$). Large intrinsic variability (with respect to measurement errors) will tend to produce a large SNR2. While there is no rigorous cut on SNR2 for robust detection of intrinsic variability, we recommend a threshold value of SNR2 > 20 for a confident detection.

In the main catalog described in Section 5.1 and Table 2, we compile the intrinsic rms variability for the continuum flux at several wavelengths and for major broad lines. We also compile the fractional rms variability relative to the average flux of the continuum and broad lines. However, we caution that the intrinsic variability may be overestimated if the feature is near the red edge of the spectral coverage, where significant sky line residuals are difficult to remove (see Figure 7).

Overall, the intrinsic fractional rms spectral variability for the continuum and broad lines is at the ~10% level during the 2014 monitoring. Given the ~5% systematic uncertainty in our flux calibration (Shen et al. 2015a), many quasars in our sample have well-detected spectral variability.

5. Catalog Format

5.1. Main Catalog

Table 2 provides the details of the compiled quasar properties and the catalog format. The associated data are provided in an online FITS file. For each measured line, we report the peak wavelength, FWHM, $\log L_{\rm line}$, rest-frame EW, and the line centroid computed from pixels above 50% of the peak flux. The peak and centroid wavelengths (λ_0') were measured in the "rest frame" using the pipeline redshift ZPIP, which can be easily converted to the rest frame based on the improved redshift ZSYS, i.e., $\lambda_0 = \lambda_0'(1 + \mathrm{ZPIP})/(1 + \mathrm{ZSYS})$, where λ_0 is the line wavelength in the rest frame defined by ZSYS.

We compile single-epoch virial BH masses based on the Hβ, Mg II, and C IV lines, following fiducial recipes used in Shen et al. (2011), which use the Vestergaard & Peterson (2006) calibrations for Hβ and C IV and our own calibration in that paper for Mg II. It is straightforward to use the compiled line widths and continuum luminosities to derive virial BH masses based on any other single-epoch estimators.

For the fiducial single-epoch virial BH masses, we adopt the estimates in the preference order of Hβ, Mg II, and C IV. We refer the reader to the comprehensive review of Shen (2013) on the caveats of these different mass estimators. Bolometric luminosities are calculated from the 5100, 3000, and 1350 Å monochromatic luminosities using bolometric corrections of 9.26, 5.15, and 3.81, respectively (Richards et al. 2006a; Shen et al. 2011). We preferentially use the 3000 Å luminosity to estimate the bolometric luminosity because it has less host contamination than the 5100 Å luminosity and suffers less from reddening and variability than the 1350 Å luminosity. We calculate Eddington ratios using the fiducial BH masses. These BH masses and Eddington ratios will be updated in the future from direct RM measurements.

Using the fiducial single-epoch virial BH masses, Figure 8 compares the distribution of SDSS-RM quasars in the mass–luminosity plane with that of the SDSS-Data Release 7 (DR7) quasar sample in Shen et al. (2011). The SDSS-RM quasars are ~2 mag fainter than SDSS-DR7 quasars, and they probe slightly lower Eddington ratios (with a median Eddington ratio of ~0.1).

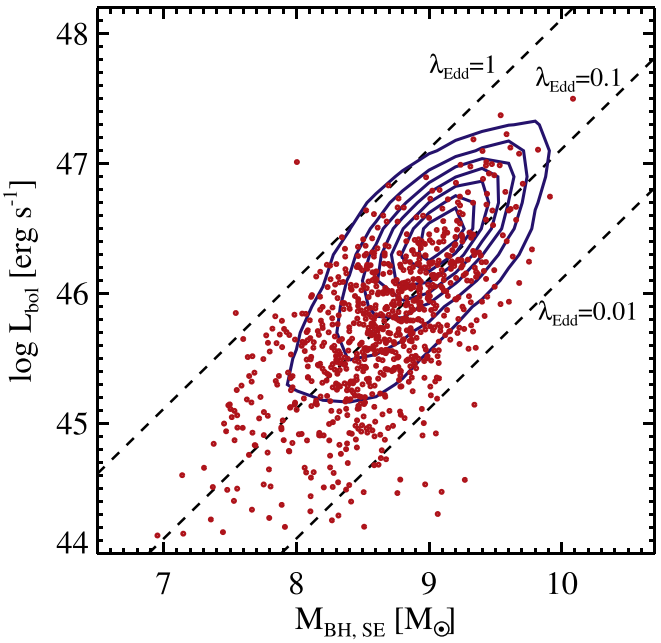

Figure 8. BH mass and luminosity plane. The SDSS-RM sample is shown as red points. The blue contours are for the SDSS-DR7 quasars compiled in Shen et al. (2011). Both samples use the single-epoch virial BH masses. The SDSS-RM quasars are, on average, ~2 mag fainter than the SDSS-DR7 sample and have smaller Eddington ratios by 0.27 dex on average. The outlier with an extreme high Eddington ratio (RMID = 785) is caused by a bad fit to a BAL quasar, which largely underestimated the C IV width and hence the single-epoch BH mass.

5.2. Supplemental Catalogs

As described in previous sections, we have compiled additional properties for the SDSS-RM sample in several ancillary catalogs. Below are the notes on these supplemental catalogs. All data files and their documentation are provided on Zenodo [doi:10.5281/zenodo.2565390] and are archived on the SDSS-RM data server.

1. *allqso_sdssrm.fits*: a FITS table of all 1214 known quasars in the 7 deg^2 SDSS-RM field. Only 849 of them received a fiber in the SDSS-RM spectroscopy. This table lists the basic target information of these quasars.
2. *QSObased_Expanded_SDSSRM_107.fits:* the narrow Mg II/Fe II absorber catalog for SDSS-RM quasars, following the methodology outlined in Zhu & Ménard (2013). Each entry corresponds to one quasar. The search for narrow absorbers includes systems that have an absorber redshift close to the quasar systemic redshift ($|\Delta z| < 0.04$). Mg II absorbers blueshifted from the quasar by $\Delta z > 0.04$ and also redward of C IV by $\Delta z > 0.02$ are of high purity. Mg II absorbers with $|\Delta z| < 0.04$, those at wavelengths blueward of C IV, or those with Fe II detection but no Mg II detections (likely due to bad pixels), while included in this catalog, should be treated with caution and may contain a small fraction of false positives (mainly C IV absorbers).

   For convenience, we also provide a version of the absorber catalog organized by absorbers (*Expanded_SDSSRM_107.fits*), i.e., each entry corresponds to one absorber system.

3. *rmqso32_aegis_multi_lambda.fits*: multi-wavelength data compiled from Nandra et al. (2015) for 32 SDSS-RM quasars in the AEGIS field.
4. *spitzer_seip_rm_match_1.5 arcsec.fits: Spitzer* IRAC and MIPS data from the *Spitzer* Enhanced Imaging Products (SEIP) source list for 176 SDSS-RM quasars, with a matching radius of 1.″5. This file also compiles infrared fluxes (if available) from the Two Micron All-Sky Survey (2MASS; Skrutskie et al. 2006).
5. *spec_2014_BALrobust.csv*: a list of 95 BALQSOs (including mini-BALQSOs) identified from the first-year coadded spectroscopy. This file includes BAL flags on C IV, Al III, Mg II, and Fe II/Fe III. It also includes notes on individual objects.
6. *PS1_MD07_LC_sdssrm.fits:* PS1 MDF light curves for the SDSS-RM quasars used to compute PS1_NMA-G_OK and PS1_RMS_MAG in the main catalog. Note this is the unofficial release of the PS1 MD07 data, which was approved by the PS1 collaboration. These photometric light curves may differ slightly from the final official release of the PS1 MDF data.

6. Summary

We presented a detailed characterization of the spectral and optical variability properties of a representative quasar sample from the SDSS-RM project. The compiled main and supplemental catalogs will serve as the basis for future SDSS-RM work that studies quasars and their host galaxies.

The SDSS-RM sample probes a diverse range in quasar properties over a broad redshift range of $0.1 < z < 4.5$. The high-S/N coadded spectroscopy allowed robust measurements of the spectral properties, and the multi-epoch spectroscopic data provided important constraints on the spectral variability of our sample.

Many SDSS-RM quasars have well-detected variability in their continuum and broad emission lines, which is a necessary (but not sufficient) condition for lag measurements.

The SDSS-RM project will continue to carry out monitored imaging and spectroscopy through 2020, as well as other dedicated multi-wavelength follow-up programs in the same field. These future data sets will provide additional information on the quasar sample and will be included in future data releases of SDSS-RM.

We thank the anonymous referee for comments that improved the manuscript. Y.S. acknowledges support from an Alfred P. Sloan Research Fellowship and NSF grant AST-1715579. P.H. acknowledges support from the Natural Sciences and Engineering Research Council of Canada (NSERC), funding reference number 2017-05983. W.N.B. acknowledges support from NSF grant AST-1516784. C.J.G., W.N.B., and D.P.S. acknowledge support from NSF grant AST-1517113. Funding for SDSS-III has been provided by the Alfred P. Sloan Foundation, the Participating Institutions, the National Science Foundation, and the U.S. Department of Energy Office of Science. The SDSS-III website is http://www.sdss3.org/.

SDSS-III is managed by the Astrophysical Research Consortium for the Participating Institutions of the SDSS-III Collaboration including the University of Arizona, the Brazilian Participation Group, Brookhaven National Laboratory, University of Cambridge, Carnegie Mellon University, University of Florida, the French Participation Group, the German Participation Group, Harvard University, the Instituto de Astrofisica de Canarias, the Michigan State/Notre Dame/JINA Participation Group, Johns Hopkins University, Lawrence Berkeley National Laboratory, Max Planck Institute for Astrophysics, Max Planck Institute for Extraterrestrial Physics, New Mexico State University, New York University, The Ohio State University, Pennsylvania State University, University of Portsmouth, Princeton University, the Spanish Participation Group, University of Tokyo, University of Utah, Vanderbilt University, University of Virginia, University of Washington, and Yale University.

Appendix
Details of the Spectral Fitting Code (QSOFIT)

Here, we provide a brief user's guide to the spectral fitting code (`qsofit`; Shen 2019) that was used to measure spectral properties of SDSS-RM quasars, which is a general-purpose code for quasar spectral fits. The code is written in IDL; a python version of the code has been developed and made public (Guo et al. 2018). The package includes the main routine, Fe II templates, an input line fitting parameter file, and ancillary routines used to extract spectral measurements from the fits. Monte Carlo estimation of the measurement uncertainties of the fitting results can be conducted with the same fitting code. The software requires the installation of the *idlutils* package,[24] which includes the widely used MPFIT IDL package (Markwardt 2009) to perform the χ^2 minimization.

The code takes an input spectrum (the observed-frame wavelength, the flux density, and error arrays) and the redshift as input parameters, performs the fitting in the rest frame, and outputs the best-fit parameters and QA plots to the paths specified by the user. The fitting results are stored as a binary table in an IDL structure format. The input flux density and errors are assumed to be in units of 10^{-17} erg s^{-1} cm^{-2} Å^{-1} per the SDSS default. Since the fitting is performed in the rest frame of the quasar, the model spectrum (f_λ) should be multiplied by $(1+z)$ when computing the monochromatic continuum luminosity λf_λ or the integrated line luminosity.

The code uses an input line fitting parameter file (qsoline*.par) to specify the fitting range and parameter constraints of the individual emission-line components. An example of such a file is provided in the package. Within the code, the user can switch on/off components to fit to the pseudo-continuum. For example, for some objects, the UV/optical Fe II emission cannot be well constrained, and the user can exclude this component in the continuum fit. The code is highly flexible and can be modified to meet the specific needs of the user. For example, if a local fit around certain emission lines is required rather than a global fit, the user can truncate the input spectrum before feeding it to `qsofit`.

An example calling sequence of fitting to a quasar spectrum is

```
IDL> qsofit, wave_obs, flux, err, z, /psplot, /fits, emparfile='qsoline.par.'
```

The package also provides several sub-routines to compute the spectral quantities from the model fits:

1. reconstruct the pseudo-continuum flux (Fe II excluded):

```
IDL> para=mrdfits('output.fits',1) %
```

[24] http://www.sdss3.org/dr8/software/idlutils.php

```
read the fits structure output by qsofit
    IDL> conti_fit=para.conti_fit % parameter array for the pseudo-continuum fit
    IDL>    conti_flux=f_conti_only(wave, conti_fit[6:*]) % the first 6 elements in contifit are reserved for the FeII model;
```

2. reconstruct the Fe II flux:

```
    IDL> f_FeII_uv=fe_flux_mgii(wave, conti_fit[0:2])
    IDL>  f_FeII_opt=fe_flux_balmer(wave, conti_fit[3:5]);
```

3. reconstruct the model line flux:

```
    IDL> line_fit=para.line_fit % parameter array for the emission line fit
    IDL> linename=para.linename % get the corresponding line names
    IDL>    ind=where(strmatch(linename, 'CIV')) % indices for the CIV line
    IDL> pp=line_fit[ind]
    IDL>  line_flux=manygauss(alog(wave), pp) % model line flux;
```

4. and obtain line properties from the multi-Gaussian fit:

```
    IDL>  result=get_multi_gaussian_prop(pp,/diet)
    % peak wavelength=exp(result[0])
    % FWHM=result[1]*3d5
    % line flux=result[2]*(1+z); in units of 10^-17 erg s^-1cm^-2
    % top 50% flux centroid=exp(result[5]).
```

ORCID iDs

Yue Shen https://orcid.org/0000-0003-1659-7035
Patrick B. Hall https://orcid.org/0000-0002-1763-5825
Keith Horne https://orcid.org/0000-0003-1728-0304
Guangtun Zhu https://orcid.org/0000-0002-7574-8078
Ian McGreer https://orcid.org/0000-0002-3461-5228
Jonathan R. Trump https://orcid.org/0000-0002-1410-0470
Karen Kinemuchi https://orcid.org/0000-0001-7908-7724
W. N. Brandt https://orcid.org/0000-0002-0167-2453
Paul J. Green https://orcid.org/0000-0002-8179-9445
C. J. Grier https://orcid.org/0000-0001-9920-6057
Hengxiao Guo https://orcid.org/0000-0001-8416-7059
Luis C. Ho https://orcid.org/0000-0001-6947-5846
Yasaman Homayouni https://orcid.org/0000-0002-0957-7151
Linhua Jiang https://orcid.org/0000-0003-4176-6486
Jennifer I-Hsiu Li https://orcid.org/0000-0002-0311-2812
Eric Morganson https://orcid.org/0000-0001-7180-109X
Gordon T. Richards https://orcid.org/0000-0002-1061-1804
Ken Chambers https://orcid.org/0000-0001-6965-7789
Nick Kaiser https://orcid.org/0000-0001-6511-4306
Eugene Magnier https://orcid.org/0000-0002-7965-2815
Christopher Waters https://orcid.org/0000-0003-1989-4879

References

Assef, R. J., Stern, D., Kochanek, C. S., et al. 2013, ApJ, 772, 26
Blandford, R. D., & McKee, C. F. 1982, ApJ, 255, 419
Blanton, M. R., Bershady, M. A., Abolfathi, B., et al. 2017, AJ, 154, 28
Boroson, T. A., & Green, R. F. 1992, ApJS, 80, 109
Cardelli, J. A., Clayton, G. C., & Mathis, J. S. 1989, ApJ, 345, 245
Chen, K., Halpern, J. P., & Filippenko, A. V. 1989, ApJ, 339, 742
Davis, M., Guhathakurta, P., Konidaris, N. P., et al. 2007, ApJL, 660, L1
Dawson, K. S., Schlegel, D. J., Ahn, C. P., et al. 2013, AJ, 145, 10
Denney, K. D., Horne, K., Brandt, W. N., et al. 2016a, ApJ, 833, 33
Denney, K. D., Horne, K., Shen, Y., et al. 2016b, ApJS, 224, 14
Eisenstein, D. J., Weinberg, D. H., Agol, E., et al. 2011, AJ, 142, 72
Eracleous, M., & Halpern, J. P. 1994, ApJS, 90, 1
Gezari, S., Martin, D. C., Forster, K., et al. 2013, ApJ, 766, 60
Gibson, R. R., Jiang, L., Brandt, W. N., et al. 2009, ApJ, 692, 758
Grier, C. J., Hall, P. B., Brandt, W. N., et al. 2015, ApJ, 806, 111
Grier, C. J., Trump, J. R., Shen, Y., et al. 2017, ApJ, 851, 21
Gunn, J. E., Siegmund, W. A., Mannery, E. J., et al. 2006, AJ, 131, 2332
Guo, H., Shen, Y., & Wang, S. 2018, PyQSOFit: Python Code to Fit the Spectrum of Quasars, Astrophysics Source Code Library, ascl:1809.008
Hemler, Z. S., Grier, C. J., Brandt, W. N., et al. 2019, ApJ, 872, 21
Homayouni, Y., Trump, J. R., Grier, C. J., et al. 2018, arXiv:1806.08360
Jiang, L., Fan, X., Annis, J., et al. 2008a, AJ, 135, 1057
Jiang, L., Fan, X., Vestergaard, M., et al. 2007, AJ, 134, 1150
Jiang, L., Fan, X., & Vestergaard, M. 2008b, ApJ, 679, 962
Kaiser, N., Burgett, W., Chambers, K., et al. 2010, Proc. SPIE, 7733, 77330
Lang, D., Hogg, D. W., & Schlegel, D. J. 2016, AJ, 151, 36
Li, J., Shen, Y., Horne, K., et al. 2017, ApJ, 846, 79
Liu, X., Dittmann, A., Shen, Y., & Jiang, L. 2018, ApJ, 859, 8
MacLeod, C. L., Ivezić, Ž, Kochanek, C. S., et al. 2010, ApJ, 721, 1014
Magnier, E. A., Schlafly, E., Finkbeiner, D., et al. 2013, ApJS, 205, 20
Markwardt, C. B. 2009, in ASP Conf. Ser. 411, Astronomical Data Analysis Software and Systems XVIII, ed. D. A. Bohlender, D. Durand, & P. Dowler (San Francisco, CA: ASP), 251
Matsuoka, Y., Strauss, M. A., Shen, Y., et al. 2015, ApJ, 811, 91
Morganson, E., Green, P. J., Anderson, S. F., et al. 2015, ApJ, 806, 244
Nandra, K., Laird, E. S., Aird, J. A., et al. 2015, ApJS, 220, 10
Pâris, I., Petitjean, P., Ross, N. P., et al. 2017, A&A, 597, A79
Peterson, B. M. 1993, PASP, 105, 247
Richards, G. T., Lacy, M., Storrie-Lombardi, L. J., et al. 2006a, ApJS, 166, 470
Richards, G. T., Strauss, M. A., Fan, X., et al. 2006b, AJ, 131, 2766
Rodríguez Hidalgo, P., Hamann, F., & Hall, P. 2011, MNRAS, 411, 247
Ross, N. P., Myers, A. D., Sheldon, E. S., et al. 2012, ApJS, 199, 3
Salviander, S., Shields, G. A., Gebhardt, K., & Bonning, E. W. 2007, ApJ, 662, 131
Schlafly, E. F., Finkbeiner, D. P., Jurić, M., et al. 2012, ApJ, 756, 158
Schlegel, D. J., Finkbeiner, D. P., & Davis, M. 1998, ApJ, 500, 525
Schmidt, K. B., Marshall, P. J., Rix, H.-W., et al. 2010, ApJ, 714, 1194
Sesar, B., Ivezić, Ž, Lupton, R. H., et al. 2007, AJ, 134, 2236
Shen, J., Vanden Berk, D. E., Schneider, D. P., & Hall, P. B. 2008a, AJ, 135, 928
Shen, Y. 2013, BASI, 41, 61
Shen, Y. 2019, QSOFit: General-purpose IDL Code for Quasar Spectral Fits, v1.0, Zenodo, doi:10.5281/zenodo.2565311
Shen, Y., Brandt, W. N., Dawson, K. S., et al. 2015a, ApJS, 216, 4
Shen, Y., Brandt, W. N., Richards, G. T., et al. 2016a, ApJ, 831, 7
Shen, Y., Greene, J. E., Ho, L. C., et al. 2015b, ApJ, 805, 96
Shen, Y., Greene, J. E., Strauss, M. A., Richards, G. T., & Schneider, D. P. 2008b, ApJ, 680, 169
Shen, Y., Horne, K., Grier, C. J., et al. 2016b, ApJ, 818, 30
Shen, Y., & Liu, X. 2012, ApJ, 753, 125
Shen, Y., Richards, G. T., Strauss, M. A., et al. 2011, ApJS, 194, 45
Skrutskie, M. F., Cutri, R. M., Stiening, R., et al. 2006, AJ, 131, 1163
Smee, S. A., Gunn, J. E., Uomoto, A., et al. 2013, AJ, 146, 32
Sun, M., Trump, J. R., Shen, Y., et al. 2015, ApJ, 811, 42
Sun, M., Xue, Y., Richards, G. T., et al. 2018, ApJ, 854, 128
Tonry, J. L., Stubbs, C. W., Kilic, M., et al. 2012a, ApJ, 745, 42
Tonry, J. L., Stubbs, C. W., Lykke, K. R., et al. 2012b, ApJ, 750, 99
Trump, J. R., Hall, P. B., Reichard, T. A., et al. 2006, ApJS, 165, 1
Tsuzuki, Y., Kawara, K., Yoshii, Y., et al. 2006, ApJ, 650, 57
van der Marel, R. P., & Franx, M. 1993, ApJ, 407, 525
Vanden Berk, D. E., Richards, G. T., Bauer, A., et al. 2001, AJ, 122, 549
Vanden Berk, D. E., Shen, J., Yip, C.-W., et al. 2006, AJ, 131, 84
Vestergaard, M., & Peterson, B. M. 2006, ApJ, 641, 689
Vestergaard, M., & Wilkes, B. J. 2001, ApJS, 134, 1
White, R. L., Becker, R. H., Helfand, D. J., & Gregg, M. D. 1997, ApJ, 475, 479
Wright, E. L., Eisenhardt, P. R. M., Mainzer, A. K., et al. 2010, AJ, 140, 1868
Yue, M., Jiang, L., Shen, Y., et al. 2018, ApJ, 863, 21
Zhu, G., & Ménard, B. 2013, ApJ, 770, 130